SOFT WHOLE ARM ROBOT SKIN

A Dissertation

Presented to the Faculty of the Graduate School

of Cornell University

in Partial Fulfillment of the Requirements for the Degree of

Master of Science

by

Boxin Xu

December 2023

SOFT WHOLE ARM ROBOT SKIN

Boxin Xu

Cornell University 2023

Whole-body tactile sensing is essential for humans to perform activities of daily living (ADLs). To enable robots to safely interact with the environment and assist humans with ADLs, a soft tactile whole-arm sensing robotic skin provides both passive and active protection. This work presents the design and fabrication of the soft fabric-based capacitive skin. The whole-arm robotic skin's performance under different resolutions, contact areas, and amount stretched are evaluated. The skin is implemented on a robot arm to perform an assistive limb repositioning task in a user study. The result shows that our soft skin adds comfort and safety to the physical human-robot interaction.

Keywords: Force and Tactile Sensing; Touch in HRI; Physical Human-Robot Interaction

BIOGRAPHICAL SKETCH

Boxin Xu was born on January 7, 1999, in a small town in Zhejiang province, China. Until the age of four, she lived with her aunt in Zhejiang before relocating to Chongqing, China, with her parents, where she completed her junior high school education. In 2016, she made the move to New York, settling in Queens and successfully finishing her high school studies.

Throughout her high school years, Boxin demonstrated a profound interest in engineering, which she passionately pursued as she furthered her education. Her insatiable thirst for knowledge led her to attain a Bachelor of Science degree in Mechanical Engineering, with a double major in Aerospace Engineering, from the University at Buffalo.

During her undergraduate years, she actively engaged in laboratory work and research under the guidance of Dr. Jiyeon Kang. Her fascination with biomedical robotics and biomechanics grew during this time, fueling her desire to apply engineering principles to solve real-world issues.

Following her graduation, Boxin initially embarked on a career as a design engineer. However, driven by her unwavering passion for robotics research, she made the decision to pursue further studies at Cornell University. Over the course of two years, she dedicated herself to researching robotics skin aimed at aiding individuals with motor disabilities in their daily activities.

Beyond her academic and professional pursuits, Boxin possesses a deep love for outdoor sports, particularly backpacking and skiing. Her dedication to these interests led her to acquire certification as a ski instructor while pursuing her master's degree.

Boxin Xu's journey exemplifies her relentless pursuit of knowledge, her commitment to innovative research in the field of robotics, and her love for outdoor

activities, all of which contribute to her multifaceted personality and endeavors.

ACKNOWLEDGEMENTS

First and foremost, I would like to express my deepest gratitude to my advisor, Dr. Tapomayukh Bhattacharjee, for his unwavering support, guidance, and mentorship throughout the course of this research. His insights, expertise, and patience have been invaluable to my academic journey, and I am truly fortunate to have had him as my guide.

I would also like to extend my heartfelt appreciation to Dr. Elizabeth Farrell Helbling and Dr. Cindy Kao, who as committee members, have provided critical feedback, encouragement, and a broader perspective to my work. Their expertise and constructive critiques have been instrumental in shaping this thesis to its current form.

To the team members, Grace Zhang, Luoyan Zhong, Xiaoyu Liang, Diego Virtue, Rishabh Madan, and Aparajito Saha: working alongside such dedicated and talented individuals has been both enlightening and rewarding. Their dedication, camaraderie, and unique perspectives have enriched the collective efforts and made this journey memorable.

Acknowledgment is also given to all the members of the EmPRISE lab. The collective wisdom, support, and collaborative spirit of the lab have fostered an environment conducive to learning and innovation. Gratitude is felt for the countless discussions, both formal and informal, that have contributed to growth as a researcher.

In conclusion, this thesis stands as a testament to many's collective efforts, guidance, and support. Deep indebtedness is felt to each individual who made this journey both challenging and rewarding. Thank you.

TABLE OF CONTENTS

Biographical Sketch . . . iii
Acknowledgements . . . v
Table of Contents . . . vi
List of Tables . . . vii
List of Figures . . . viii

1 Introduction **1**
1.1 Literature Review . . . 2
1.1.1 Small-area tactile sensors . . . 2
1.1.2 Large-area tactile sensors . . . 3

2 Large Scale Soft Robot Skin **5**
2.1 Sensor Design and Fabrication . . . 5
2.1.1 Validation of Concept . . . 8
2.1.2 Stretchable Taxel . . . 11
2.1.3 Cushioning Effect Material . . . 12
2.1.4 Soft bubble as dielectric layer . . . 13
2.1.5 Squishy as dielectric layer . . . 17
2.2 Sensor Circuit Design . . . 20
2.2.1 Hardware shielding . . . 22
2.3 Data Workflow . . . 23
2.3.1 Calibration . . . 23
2.3.2 Signal Filter . . . 24
2.3.3 Data Visualization . . . 24
2.4 Skin Characterization . . . 25
2.4.1 Sensor Characteristics and Performance Evaluation . . . 26
2.4.2 Comparative Analysis of Alternative Designs . . . 28
2.5 Capacitance Modeling And Validation . . . 30
2.6 User Study . . . 34
2.6.1 Experimental Setup . . . 35
2.6.2 Experimental Procedure . . . 35
2.6.3 Results and Discussion . . . 36

3 Conclusions and Future Directions **37**
3.0.1 Conclusion . . . 37
3.0.2 Future Work . . . 37

A Appendix A **39**

LIST OF TABLES

2.1 Dielectric Constant of Materials 6
2.2 Taxel materials 19

LIST OF FIGURES

2.1 Schematic Capacitive Sensor Circuit [1] 7
2.2 Sewing Pattern of Ring Connector: Number representing the thread sequence. 9
2.3 Taxel and Outter Layer Cutting Process 10
2.4 A Taxel in Real World 11
2.5 The Soft bubble 14
2.6 Polymer Casting Procedure 15
2.7 **Whole Arm Soft Stretchable Robot Skin.** We cover a robot arm with CushSense to perform the pHRI task of limb manipulation. CushSense comprises closely arranged, soft taxels (**tac**tile pix**el**s) that conform to the shape of the robot and objects it interacts with, accurately sensing forces upon contact. It uses pliable and stretchable materials, allowing each layer to stretch while maintaining reliable sensing and ensuring both force sensing and comfort. 17
2.8 **Whole-arm Skin Structure**. (a) A taxel, with 9 layers, acts as a capacitive sensor. (b) We made a skin section for each link of the robot arm, where each taxel measures a capacitance value. (c) We daisy-chain the skin sections to build a whole-arm skin comprising 56 taxels. (d) An Arduino board collects data and publishes it to a ROS topic, which is used by a calibration function to estimate contact forces, shown on a 3D model of the robot in RViz. 18
2.9 Simplified Connection for One Microcontroller 21
2.10 **Sensor Characteristics and Performance Evaluation.** The top-left corner of (a) shows the experiment setup comprising F/T Sensor (in light gray), Indenter (in dark gray), and the taxel (in purple). Experiment (a) validates the force-sensing capability of our skin, (b) exhibits minimal hysteresis error, (c)-(d) shows reduction of noise due to electric interference, and (e)-(f) retains sensitivity under compression and deformation. 25
2.11 **Comparative Analysis with Alternative Designs**. Experiments (a)-(b) illustrate that Squishy as a dielectric maximizes sensitivity. Smaller taxels exhibit further increases in sensitivity (c). We chose a taxel size of 4x4 cm based on a tradeoff between sensitivity and ease of construction. 29
2.13 **Model-based Filtering.** Comparison of ground truth forces with skin data and the math model processed data. The processed data is obtained using *filtered* = 0.4 * *analytical* + 0.6 * *measured*, where *analytical* is calculated using the math model and *measured* is the skin data. The processed data demonstrates reduced noise and aligns well with ground truth. 33

2.14 **User Study and Analysis.** Experimental setup, study procedure, and results from the limb manipulation user study evaluating the two skins' perceived safety and comfort. Most participants preferred the Cush Material over the Scuba Fabric. *** indicates significant differences with $p_{0.0001}$. 33

CHAPTER 1

INTRODUCTION

According to a 2021 report [2], over a billion individuals globally require assistance with activities of daily living (ADLs) such as bathing and dressing. Caregiving robots have the potential to assist these individuals, but some tasks, such as dressing and transferring, require contacts across the entire robot arm, which poses challenges [3]. Addressing this challenge is essential to improve the utility of caregiving robots. A promising approach is the integration of whole-arm tactile skins on robot arms. These skins can provide detailed information about contacts, promoting safer physical interactions. Moreover, these sensors are not limited to caregiving; they are valuable when operating in unstructured environments where frequent whole-arm contacts are inevitable, for instance, when retrieving objects from cluttered spaces [4]. An ideal tactile skin for physical human-robot interaction (pHRI) should be soft, offering both active protection through compliant control [5] and passive protection, provided by hardware, for increased comfort. Furthermore, the skin should be stretchable, allowing coverage around the robot joints [6], even during changes in the robot configuration. To enable contact-rich interactions, it should also provide good spatial and temporal resolution. Lastly, the sensor should be modular and cost-effective, ensuring its adaptability and accessibility as an open-source technology across a broad spectrum of robotic applications.

While rigid whole-arm tactile skins [7, 8] have shown efficacy in manipulating large objects and detecting obstacles in unstructured environments, they fall short in softness and stretchability. Finding materials that combine these qualities without compromising sensing capabilities is challenging. Fabric-based

skin sensors [6, 9] offer some promise, but many existing designs lack the requisite softness and cushioning for pHRI. Also, the large-scale nature of these skins introduces additional complexities. Due to their extensive coverage area and potential for multiple interaction points, these sensors are inherently more prone to noise from environmental interference, crosstalk, etc. Lastly, the scale of these sensors presents challenges in efficient fabrication, user-friendly assembly, and managing data latency.

1.1 Literature Review

Tactile sensing is becoming increasingly important in robotic systems, enabling robots to execute tasks such as object recognition [10], grasping [11], and uneven terrain locomotion [12] using small-area tactile sensors. These sensors also facilitate whole-arm [3, 4] and whole-body [5, 13] manipulation tasks with large-area tactile sensors.

1.1.1 Small-area tactile sensors

Prior research has explored various sensing principles for building small-area tactile sensors. Among these are magnetic-based sensors, introduced by [14–19]. These sensors detect force changes by tracking magnetic field fluctuations using magnetometers. They exhibit high precision, sensitivity, and resolution, as well as can be made soft by incorporating magnetic particles into silicone gel. Vision-based sensors proposed by [20–24] employ RGB cameras or other imaging devices behind a translucent membrane. This setup captures tactile feed-

back as the membrane deforms. Such sensors offer the advantages of high spatial resolution and resistance to electrical disturbances. Capacitive sensors developed in [25–28] function by measuring electric field changes, typically arising from variances in electrode distances. They are highly sensitive and incorporate soft materials for electrode molds. Similarly, fluid-based sensors [29–32] detect force changes by sensing voltage variations arising from alterations in the cross-sectional area of the liquid channel under applied force. While small-area tactile sensors have demonstrated potential for extension to large areas, they face scalability issues, primarily due to intricate and costly fabrication processes [17, 27]. Some of these sensors are cost-efficient and easy to fabricate, but their rigid and bulky design [16, 20, 21] renders them less suitable for pHRI applications that require whole-arm tactile sensing.

1.1.2 Large-area tactile sensors

The development of large-area tactile skins employs similar principles from small-area sensors and introduces methods apt for large-area sensing. Piezoresistive skin sensors, as discussed in [33–39], detect force changes via voltage variations from piezoelectric materials under pressure. Resistive skin sensor in [9] monitors force change through various contact areas under pressure. Although these sensors adapt to curved robot surfaces, many either lack the desired softness or the passive compliance crucial for pHRI [35, 39, 40]. Capacitance-based tactile sensors, presented in [41–43], offer cost benefits, but existing sensors are not as stretchable. Also, some capacitive artificial skins are unable to detect non-conductive objects[44]. Air-inflated skins, proposed in [13, 45–47], monitor air pressure changes to detect forces. While they provide

passive compliance, they have low spatial resolution and do not cover joints well. Vision-based, large-area skins [48, 49] tackle the issue of data management by mounting two cameras per link (top and bottom) to track marker displacements on a soft mold wrapped around the link. While these skins exhibit high spatial resolution and are soft, they fall short in joint coverage and lack the cushioning essential for comfortable pHRI. Current research has yet to achieve a holistic solution meeting all pHRI demands in softness, stretchability, comfort, and spatial resolution. Our proposed research seeks to address this gap.

CHAPTER 2

LARGE SCALE SOFT ROBOT SKIN

To bridge the gap between existing work and address all pHRI demands, we embarked on designing and fabricating a large-scale, soft, stretchable skin featuring a spatial resolution of 4x4 cm. The user study conducted in 2.6 confirms the skin's comfort in pHRI interactions. This chapter extensively outlines the skin's design and fabrication process, encompassing circuit and hardware design, as well as data structure. Additionally, a comprehensive series of characterizations were performed, alongside a user study, to substantiate the skin's comfort during pHRI task limp repositioning.

2.1 Sensor Design and Fabrication

Among textile-based sensors, both resistive and capacitive technologies have been popular choices. However, compared with resistive textile sensors, capacitive textile sensors have the advantages of higher linearity, sensitivity, and less hysteresis[50]. A typical capacitive sensor comprises two conductors separated by a dielectric layer. For the stretchable conductors, conductive fabric is employed due to its breathable, skin-safe, and stretchable properties. To select an apt dielectric layer, it's imperative to comprehend the capacitance principle equation:

$$C = \frac{\epsilon A}{d} \tag{2.1}$$

Where C, ϵ, A, and d denote capacitance, relative permittivity, overlapped electrode area, and distance between electrodes, respectively. Assuming each sensor comprises two perfectly parallel plates, A remians constant. The equation underscores that capacitance is influenced by both ϵ and d, which correlate to the

material's dielectric constant and thickness. Various materials with differing dielectric constants ϵ. were explored for the dielectric layer, including Polydimethylsiloxane (PDMS), Nylon spandex fabric, rubber, and Neoprene.

Table 2.1: Dielectric Constant of Materials

Materials	Dilectric Constant
PDMS	2.3-2.8 [51]
Nylon Spandex Fafric	5.3 [52]
Rubber	2.35 [53]
Neoprene	9.8 [53]

The composite fabric's dielectric constant was determined using the Maxwell-Garnett Model:

$$\epsilon_{eff} = \epsilon_m \left(\frac{1 + 2f\left(\frac{\epsilon_i - \epsilon_m}{\epsilon_i + 2\epsilon_m}\right)}{1 - f\left(\frac{\epsilon_i - \epsilon_m}{\epsilon_i + 2\epsilon_m}\right)} \right) \tag{2.2}$$

Where ϵ_{eff} represents the effective dielectric constant, ϵ_m is the matrix material's dielectric constant, ϵ_i is the inclusion material's dielectric constant, and f is the volume fraction of ϵ_i.

These materials' dielectric constants are shown in Table 2.1.

To test how materials perform as a capacitive sensor, the Arduino's CapacitiveSensor library was utilized..

In the circuit design as shown in Fig. 2.1, the CapacitiveSensor function alters the state of a microcontroller's (MC) sending pin and subsequently monitors the receiving pin to match the same state. Within a while loop, a variable is increased to measure the duration until the receiving pin matches the sending pin's state change. The function then returns this variable's value in an arbi-

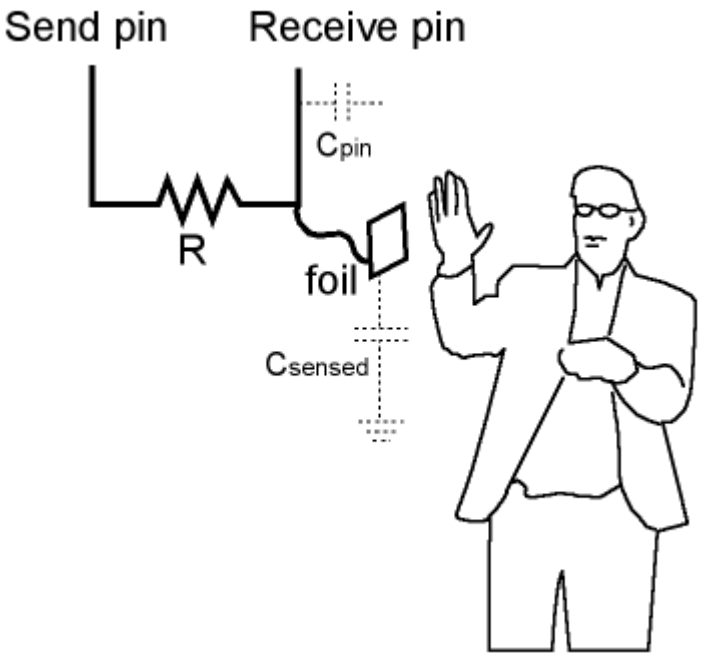

Figure 2.1: Schematic Capacitive Sensor Circuit [1]

trary unit. The human in the figure is assumed to be grounded, with air acting as the default dielectric layer between the foil and the human hand. This dielectric layer was substituted with the materials listed in Table2.1 for performance testing.

Results indicate that materials with a higher dielectric constant produce greater capacitance, which correlates with the arbitrary number in Arduino. Given that $\tau = RC$, the time constant τ is directly proportional to capacitance. Materials with a higher dielectric constant also exhibit increased latency compared to those with a lower constant. They also demonstrate heightened sensitivity and noise. It was observed that larger taxels (**tac**tile pix**el**s) are more prone to noise than smaller ones. Similarly, longer wires accumulate more noise than shorter ones, irrespective of the insulation materials. However, insulated wires yield clearer results than their non-insulated counterparts. A pivotal observation was that the sensor primarily responded to human touch. This is logical

since non-conductive objects cannot function as another plate in Fig.2.1, rendering their touch undetectable.

2.1.1 Validation of Concept

Nonetheless, the objective is to design a sensor that can detect not just human touch but also interactions with surrounding objects. To achieve this capability, enabling the skin to sense both conductive and non-conductive objects became essential. We modified the circuit in Fig.2.1 by introducing another piece of conductive fabric layer to replace the human hand in the diagram and connecting it to the ground. Therefore, the sensor should be able to sense the force change by detecting changes in distance between two parallel conductive fabric pieces.

To validate the concept, constructed a 5-layer fabric taxel, mirroring the structure depicted in Fig.2.4. It comprises two conductive layers made of Silverell fabric, flanked by two non-conductive layers of Nylon Spandex fabric, with a single dielectric layer nestled in the center.

Fabrication Process

1. Flatten one link of the Kinova Gen3 robot arm's surface in Solidworks CAD software. This flattened surface serves as the outermost layer for the taxel section, with all taxels in one link sharing non-conductive insulation layers.
2. Design taxels in the desired shape.
3. Export the shapes and outer layers as DXF files.

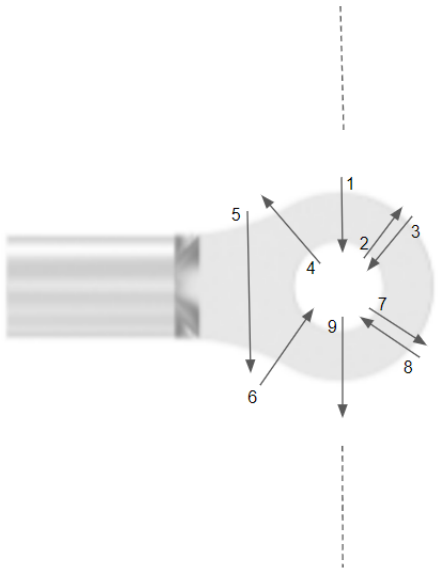

Figure 2.2: Sewing Pattern of Ring Connector: Number representing the thread sequence.

4. Laser cut the designs using the Epilog Legend 36EXT, setting power to 29% for non-conductive fabric and 27% for conductive fabric, with a speed of 50%.

5. To connect the conductive fabric to a microcontroller, fabricate special wires by crimping a ring connector to them.

6. Sew the wire with its ring connector onto the conductive fabric as illustrated in Fig. 2.2. Ensure the conductive thread is close to the metal ring for a stable connection and test after sewing.

7. Repeat for both conductive layers.

8. Sew all five fabric layers together using non-conductive thread.

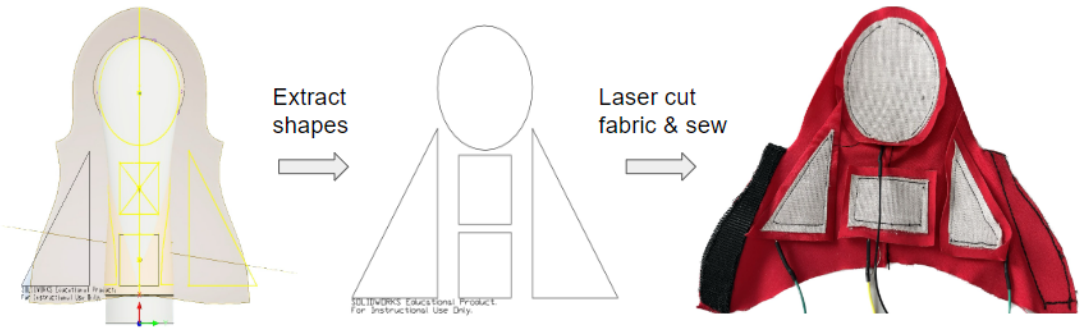

Figure 2.3: Taxel and Outter Layer Cutting Process

Discussion

We observed that the skin exhibits significant changes upon contact with humans, while changes are minimal with non-conductive materials. One notable feature of capacitive sensors is their ability to sense proximity. This is attributed to the human body acting as an electrode, which introduces changes to the electric field. Ideally, differentiating between human touch and environmental contact would be beneficial. However, challenges arise in distinguishing between light human touches and heavy presses from non-conductive materials due to overlapping regions. For instance, a light touch from a non-conductive material might produce readings similar to those of proximity sensing. Additionally, the sensor's signal becomes noisy in the presence of nearby electrical circuits. For example, when the skin is applied to the robot arm or when using an F/T sensor for touch, the sensor picks up significant noise from the circuits within the F/T sensor and robot arm. This noise persists even when the robot arm is powered off, as long as it remains connected to a power cable. These observations suggest that the skin requires a filter to refine the signal.

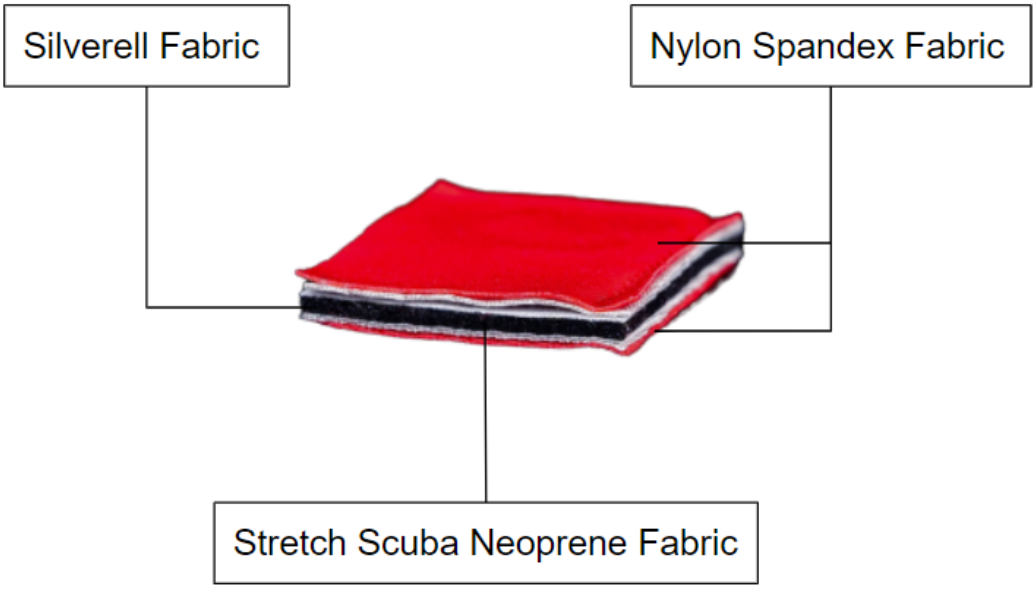

Figure 2.4: A Taxel in Real World

2.1.2 Stretchable Taxel

Building on the previously mentioned challenges, a potential solution to ensure accurate force readings, regardless of whether the touch is from a human or a non-conductive object, is to amplify the capacitance change. As indicated by Eqn. 2.1, a broader range in ΔC can be achieved with increasing values of Δd and ϵ. Referring to Table. 2.1, neoprene stands out with the highest dielectric constant. The commercial market offers a variety of neoprene products, including neoprene rubber sheets, sponge foam, and scuba fabric. Prioritizing stretchability and softness for the skin, scuba fabric was chosen as the dielectric layer. The fabrication process remains the same with the methodology detailed in 2.1.1.

A notable advantage of scuba fabric is its accessibility and cost-efficiency, especially when compared to other dielectric materials such as PDMS. It is cost-

effective as an off-the-shelf product. For instance, a yard was priced at 20 US Dollars from Joann, sufficient for whole-arm coverage. Additionally, its thickness surpasses that of Nylon spandex fabric, providing a great change in the distance between two electrodes.

2.1.3 Cushioning Effect Material

While the Scuba fabric is 4mm thick, it doesn't match the softness of air-inflated sleeves [13, 46]. These skins are sufficiently thick to offer a cushioning effect during human interaction. In pHRI, the buffer against collisions between humans and the rigid robot structure relies solely on material thickness. Thus, the search began for materials that could provide this cushioning effect.

Shipping air bubbles were initially considered. Both small and large bubbles were tested for their protective capabilities using an egg. The egg, wrapped in both small and large shipping bubbles, was dropped from the same height. It was observed that the larger bubbles offered superior protection due to:

1. Cushioning Effect: Larger bubbles contain more air, offering a thicker cushioning layer. This increased air volume effectively absorbs and distributes impact forces.
2. Compression Resistance: Larger bubbles resist complete compression upon impact better than smaller ones, avoid direct contact between the eggshell and hard surface.
3. Surface Area: The increased surface area of larger bubbles spreads the impact force over a wider area, reducing pressure on the protected item.

4. Shock Absorption: The ample air volume in larger bubbles ensures enhanced shock absorption, dispersing the kinetic energy of an impact and reducing the force on the protected item.

However, while shipping air bubbles are easily accessible, they are fragile and perform poorly under heat. Customizing these bubbles to fit the irregular surface of the Kinova Gen 3 proved challenging. Attempts to use heat to resize the bubbles resulted in melting and leakage. Given their thin nature and intended single-use design, a more durable alternative was sought.

Attention then turned to silicone materials used in soft robotics [54]. Tests were conducted with ecoflex 00-30 and 00-50, with the primary difference between them being stiffness. Using 3D-printed molds, hollow cubes were cast from these materials. By injecting air, the stiffness of the resultant air bubble could be controlled. Initially, the air bubble was intended solely for support, but it was discovered that the signal was clearer and more sensitive when the air bubble was used as the dielectric layer. Furthermore, if the soft bubble was only used for support, the capacitance reading would depend on both the dielectric layer and the soft bubble. There's also the potential for either the dielectric layer or the soft bubble to saturate first.

2.1.4 Soft bubble as dielectric layer

This version of the skin shares the same structure as the stretchable taxel, with the only distinction being the dielectric material. Ultimately, Ecoflex 00-30 was chosen over 00-50 due to its softer nature, allowing for more air space.

Figure 2.5: The Soft bubble

Fabrication Process

1. The soft bubble is composite in two parts. Part one in Fig.2.6 is the 5 sides wall. To make the soft bubble empty inside, we first 3D print a simple 5 sides cube mold without a lid.
2. Then print another smaller 5-sides cube mold to immerse in the large one to make the cavity.
3. Pour part A and part B of Ecoflex 00-30 (smooth-on LLC) together at the 1:1 ratio in weight.
4. Then use a centrifugal machine to help mix and eliminate small air bubbles inside the mixture.
5. Then the mixture is turned to a vacuum chamber to further extract tiny air bubbles inside the mixture.
6. Evenly spray mold realizing agent on mold, wait 5 min.
7. Repeat step 6.
8. Pour the mixture solution into the mold and send it to the furnace for 4 hours at 60 °C. Once part one is cured, we take it out of the furnace.

9. Get the solution for part two using the same procedure,
10. After pouring the solution into the mold, we put part one on part two and sent it to the furnace together. The ecoflex sillicone will bond together. After the part two cure, we get a completely soft bubble.
11. To make the soft bubble inflate to the desired state, we use a syringe needle to inject air inside the cavity, then we seal the tiny hole using Sil-Poxy (smooth-on LLC).
12. Perform steps 2-8 from the fabrication process in 2.1.1
13. After that, we attach the soft bubble with conductive fabric using Sil-Poxy.

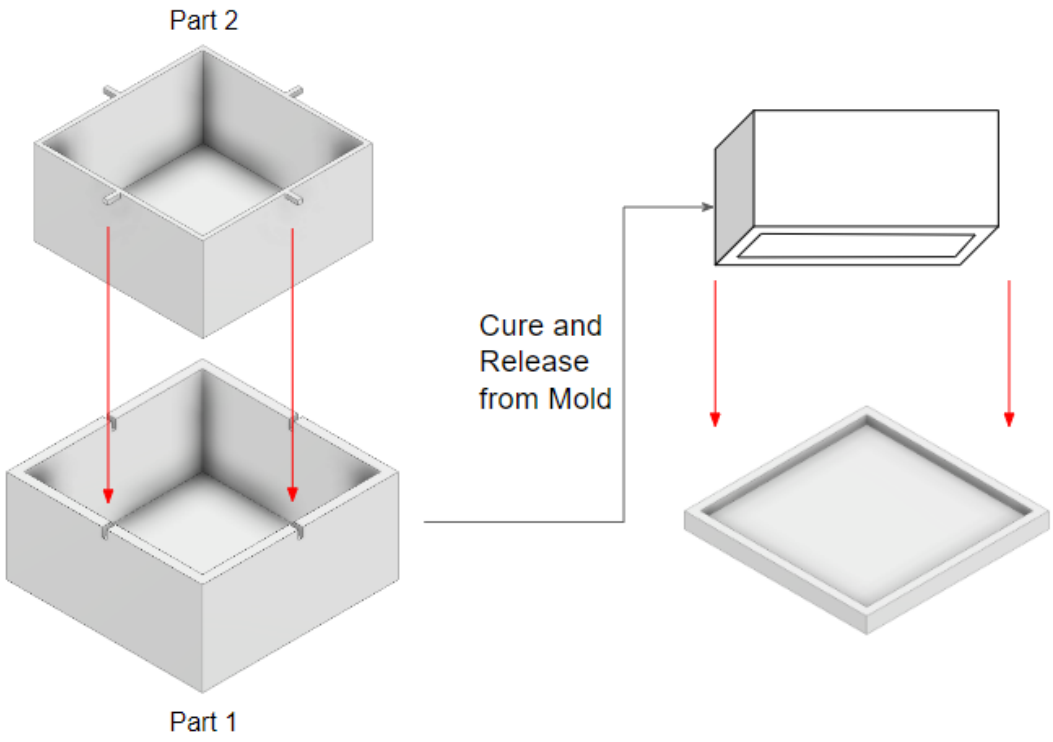

Figure 2.6: Polymer Casting Procedure

The detailed drawings of molds are included in the Appendix.A

Discussion

During the fabrication process, extracting all small air bubbles in the solution is one important step. Air bubbles inside the mixture solution will turn into the weak points of the soft bubble. The soft bubble will easily break from those weak points while injecting air and during pressing. To speed up the mold-releasing process, besides using releasing agent, an efficient way is using the dragon skin silicone from smooth-on instead of using a rigid 3D printed mold. This way could also ensure the air bubble is not broken during mold-releasing. However, we find that air leaks gradually over time, which will make the calibration function not accurate. To overcome this problem, we switched air bubble in Fig.2.5 to airless squishy material, which provides cushioning effect using structural force.

2.1.5 Squishy as dielectric layer

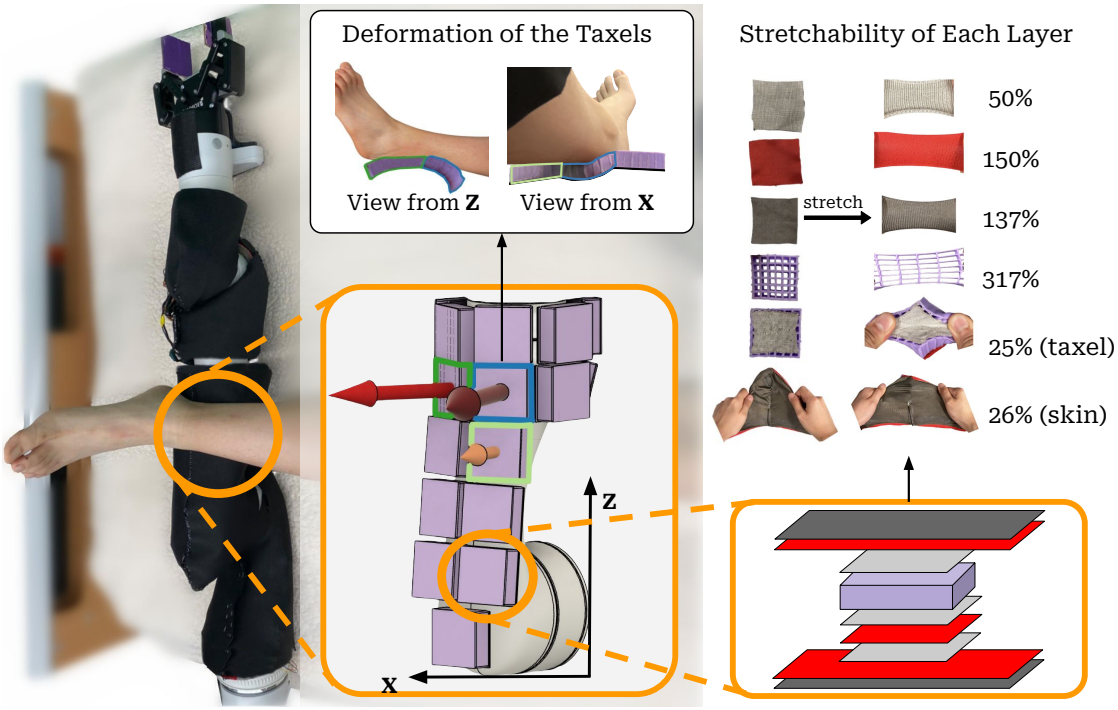

Figure 2.7: **Whole Arm Soft Stretchable Robot Skin.** We cover a robot arm with CushSense to perform the pHRI task of limb manipulation. CushSense comprises closely arranged, soft taxels (**tac**tile pix**el**s) that conform to the shape of the robot and objects it interacts with, accurately sensing forces upon contact. It uses pliable and stretchable materials, allowing each layer to stretch while maintaining reliable sensing and ensuring both force sensing and comfort.

We present *CushSense* (see Fig. 2.7), a fabric-based tactile sensing skin that is soft, stretchable, and comfortable, making it a good fit for pHRI. CushSense is comprised of taxels made from low-cost stretchable fabric, a hyper-elastic polymer that provides the cushioning effect necessary for passive compliance, making the interaction more comfortable. The skin is able to detect taxel deformations caused by applied forces through changes in capacitance. With calibration, it can identify contact position as the centers of activated taxels and the applied force values, making this sensor useful for applications that rely on tactile feedback for closed-loop control. To make the skin accessible, we used off-the-shelf cost-effective materials (~US$7 per taxel, US$387 for the whole robot arm) and

open-source fabrication methods that do not require access to specialized equipment.

In this section, we detail the design and fabrication for CushSense. We describe the construction of an individual sensing unit, known as a taxel (Sec. 2.1.5). We also present the configuration of the entire skin (Sec. 2.2), which covers different sections of a robotic arm. This modular approach allows for adapting the skin to specific application needs and facilitates easy maintenance and replacement. All design and circuit board files, fabrication details, material costs, calibration utilities, and robot operating system (ROS) packages developed for this skin are open-source [55].

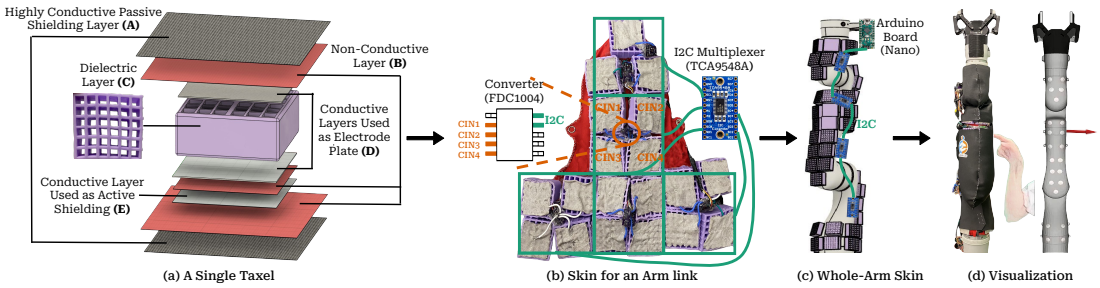

Figure 2.8: **Whole-arm Skin Structure**. (a) A taxel, with 9 layers, acts as a capacitive sensor. (b) We made a skin section for each link of the robot arm, where each taxel measures a capacitance value. (c) We daisy-chain the skin sections to build a whole-arm skin comprising 56 taxels. (d) An Arduino board collects data and publishes it to a ROS topic, which is used by a calibration function to estimate contact forces, shown on a 3D model of the robot in RViz.

An individual sensing element or taxel is made of 9 layers, which is illustrated in Fig. 2.8. Refer to Table 2.2 for a list of materials used to build the taxel. The **A** layers serve as a passive shield. The **B** layers serve as insulators to prevent the taxel from shorting. Layer **C** is a thick, Squishy dielectric layer sandwiched between two **D** layers of light, conductive fabric. The **D** layers act as two parallel plate electrodes in the capacitor. Layer **E** functions as an active

Layer	Material	Function	Composition
A	Stretch Conductive Fabric	Passive shielding and Grounding	76% Silver-coated Nylon, 24% Elastic Fiber Fabric
B	Nylon Spandex Fabric	Spacing	80% Nylon, 20% Spandex
C	Purple Squishy	Dielectric	GelFlex elastic polymer, Polyurethane foam
D	Silverell Fabric	Conductive fabric	16% Silver-coated Nylon, 84% Rayon
E	Silverell Fabric	Active shielding	16% Silver-coated Nylon, 84% Rayon

Table 2.2: Taxel materials

shield. On contact, the deformation of the taxel leads to corresponding changes in capacitance. Also, active shielding and passive shielding were added to deal with parasitic capacitance and external interference, which helps reduce sensor noise.

Fabrication Process

1. To fabricate layer **A** and **B**: flatten the surface of one link of Kinova Gen3 robot arm in Computer-Aid-Drawing (CAD) software Solidworks. (The flatterned surface is the most outer layer for the whole section of taxel. All taxels in one link of robot arm share layers **A** and **B**.)
2. Draw squares of 4x4 cm. (Draw multiple squares for massive production.)
3. Export squares and the layer **A** and **B** as DXF files from Solidworks.
4. Send the DXF file to laser cutter (Epilog Legend 36EXT).
5. Set power as 29% to cut non-conductive fabric and 27% for conductive fabric, and set speed to 50%.

6. Sew layer **A** and **B** together using non-conductive thread.
7. Crimp ring connector with wire.
8. Sew the wire with ring connector on layer **A** and **D** in the pattern shown in Fig. 2.2. Sew the conductive thread as close as possible with metal ring to ensure stable connection. And always test wire connection after sewing.
9. Use E6000 fabric glue to adhese layer **A**, **D** and **E**.
10. Use velcro to join layer **D** and **E**.

To mount CushSense on the robot arm, we use Velcro to attach the section of CushSense to itself, as shown in Fig. 2.3. In joint areas, there is a tendency for CushSense to fall off. Therefore, we use small pieces of Velcro to attach the bottom layer, **A**, to the surface of the robot arm to prevent CushSense from detaching.

For the purpose of the whole-arm skin, we fixed the taxel size to 4cm x 4cm. We carried out a series of characteristic experiments (Sec. 2.4) to choose the size, material, and design that optimizes the sensor performance for pHRI applications.

2.2 Sensor Circuit Design

We combined individual taxels with Capacitance to Digital Converters (CDCs) and custom-printed circuit boards (PCBs) to create a tactile sensing skin. The taxels are arranged on the Kinova Gen3 7 DoF robot arm, aligning precisely with its shape as shown in 2.8. We employed a modular design approach, ensuring that the taxels can be easily configured to cover specific sections of inter-

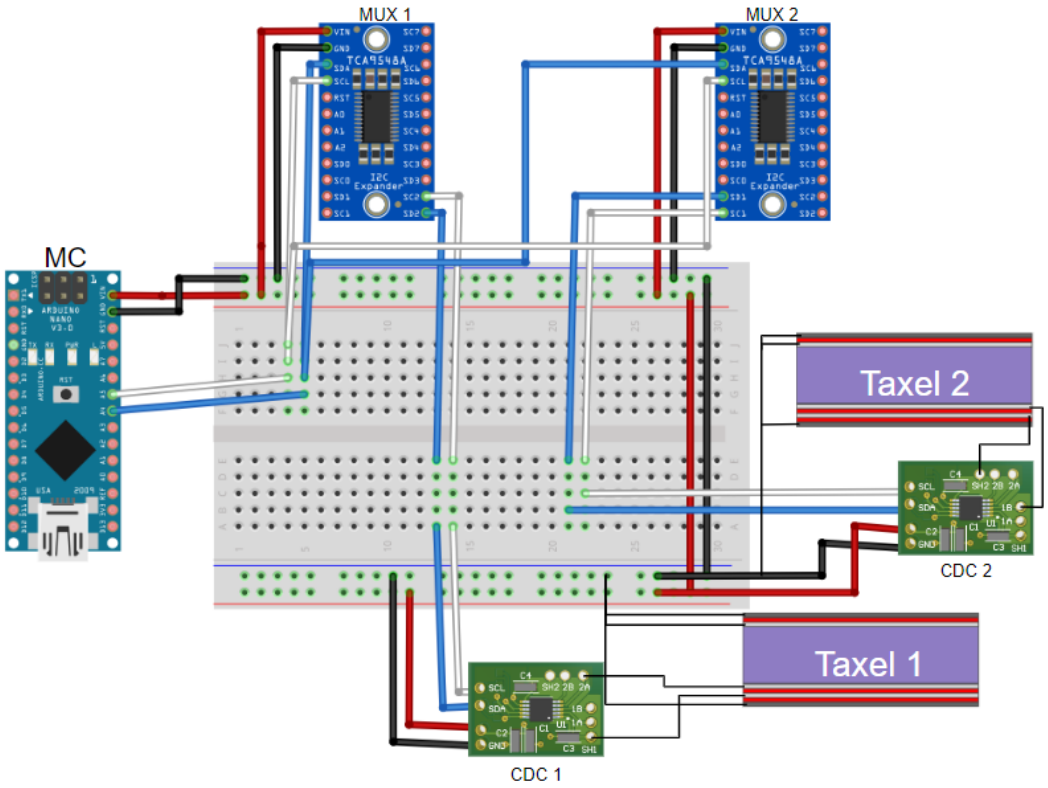

Figure 2.9: Simplified Connection for One Microcontroller

est. If taxels malfunction, users can also easily replace them by unplugging and plugging in a new one. Additionally, quick connectors are integrated into the design, connecting multiplexer or MUX with CDC boards, facilitating straightforward board replacement and the selection of specific skin sections, enhancing the overall usability and adaptability of the skin.

A simplified circuit connection is shown in Fig. 2.9. One CDC board have four ports for taxels: 1A, 1B, 2A and 2B. Connecting taxel to any of them would work. The layer **A** close to layer **E** is the sensing plate, another layer **A** connects to ground. Two active shielding ports SH1 and SH2 are shorted together in the CDC board. When connecting CDC and taxel, always use wires with same length. Because capacitive sensor is very sensitive to conductivity change. As

we mentioned in 2.1.1, use shortest wire possible between taxel and CDC to reduce noise. The PCB we designed for multiplexer have stackable design and enable the diasy chain implementation in I2C communication.

We created four sections of CushSense for the links that are most likely to come into contact with users when providing caregiving assistance [3]. Each section of the skin is made up of anywhere from 9 to 19 taxels, depending on the size of the link. To streamline data collection from the entire arm of sensors and accommodate the skin's modularity, we integrated one I2C multiplexer (Adafruit TCA9548a) for each link. Each multiplexer can support up to 7 CDCs with the same address. We leave one port empty from every multiplexer to deselect from this multiplexer to work with multiple multiplexers. Each CDC can support up to four taxels. We can specify ports to active from Arduino IDE. We choose an off-the-shelf FDC1004 CDC, a 4-channel CDC board that offers a wide capacitance range of ± 15pF and a measurement resolution of 0.5fF. It provides output rates ranging from 100-400Hz. Using a single Arduino Nano, our design is able to accommodate up to 196 taxels. Additional microcontrollers may be integrated into ROS depending on the application.

2.2.1 Hardware shielding

To enhance CushSense's reliability, sensors incorporate an active shield driver that counters electric interference from environmental sources such as robot arm electronics and humans. This is achieved by aligning the shield electrode's voltage closely with that of the sensing electrode, effectively nullifying the electric field between them and reducing parasitic capacitance. Additionally, we use a

highly conductive fabric for passive shielding against noise from the robot arm, human body, etc. This passive shield, crucial for capacitive sensors, serves as grounding insulation.

2.3 Data Workflow

2.3.1 Calibration

To calibrate the sensor, we first gather raw capacitance data from the Arduino. This data is then relayed to a Python interface via the Robot Operating System (ROS). Within ROS, the Arduino publishes sensor readings to one topic, while the F/T sensor (ATI nano25) broadcasts the ground truth force to another. For calibration, the robot arm, holding the F/T sensor, presses a single taxel on a table. Post data collection, we input the capacitance-to-force relationship into the regression model $F = a_0x^3 + a_1x^2 + a_2x + a_3$, where a_0, a_1, a_2 and a_3 are coefficients of the third-order polynomial function. With these coefficients determined, sensor data can be fitted into the function to derive force, which is then published to a new ROS topic. However, the Arduino can occasionally be inconsistent in publishing data. To ensure synchronized timestamps between capacitance and force data points, the publisher is set to release the most recent data if the Arduino stops its publishing.

2.3.2 Signal Filter

In addition to passive and active shielding, we've incorporated a low-pass filter within the Python interface to refine the signal. The Python interface subscribes to the raw skin data in the ROS topic and then channels this data through a live Butterworth low-pass filter. This filter subsequently produces a second-order sections signal. For our design, we've optimized the filter parameters to a second order with a cutoff frequency of 1.5 Hz and a sampling frequency of 60 Hz. To tare the sensor readings, we use the first 100 data points to determine an average value, which is then subtracted from each subsequent data point.

2.3.3 Data Visualization

To visualize the sensor readings, we employ Rviz, a 3D visualization tool for ROS. We begin by importing the robot's Unified Robotics Description Format (URDF) file into Rviz. Subsequently, we utilize a 3D CAD file with all taxels assembled on the arm to pinpoint each taxel's location and orientation. We then establish a point and axis perpendicular to the robot's surface at the center of each taxel. This information is compiled into a JSON file, which contains each taxel's location, as well as its roll, pitch, and yaw relative to each link. A transformation matrix then converts these locations and orientations to a global coordinate system. This approach enables the visualization to display real-time skin readings, even during the robot's motion. The visualization differentiates force using both a color map and the magnitude of length. For instance, a forceful contact is represented by a dark red, elongated arrow originating from the taxel's center, whereas a gentle press appears as a light red, shorter arrow.

2.4 Skin Characterization

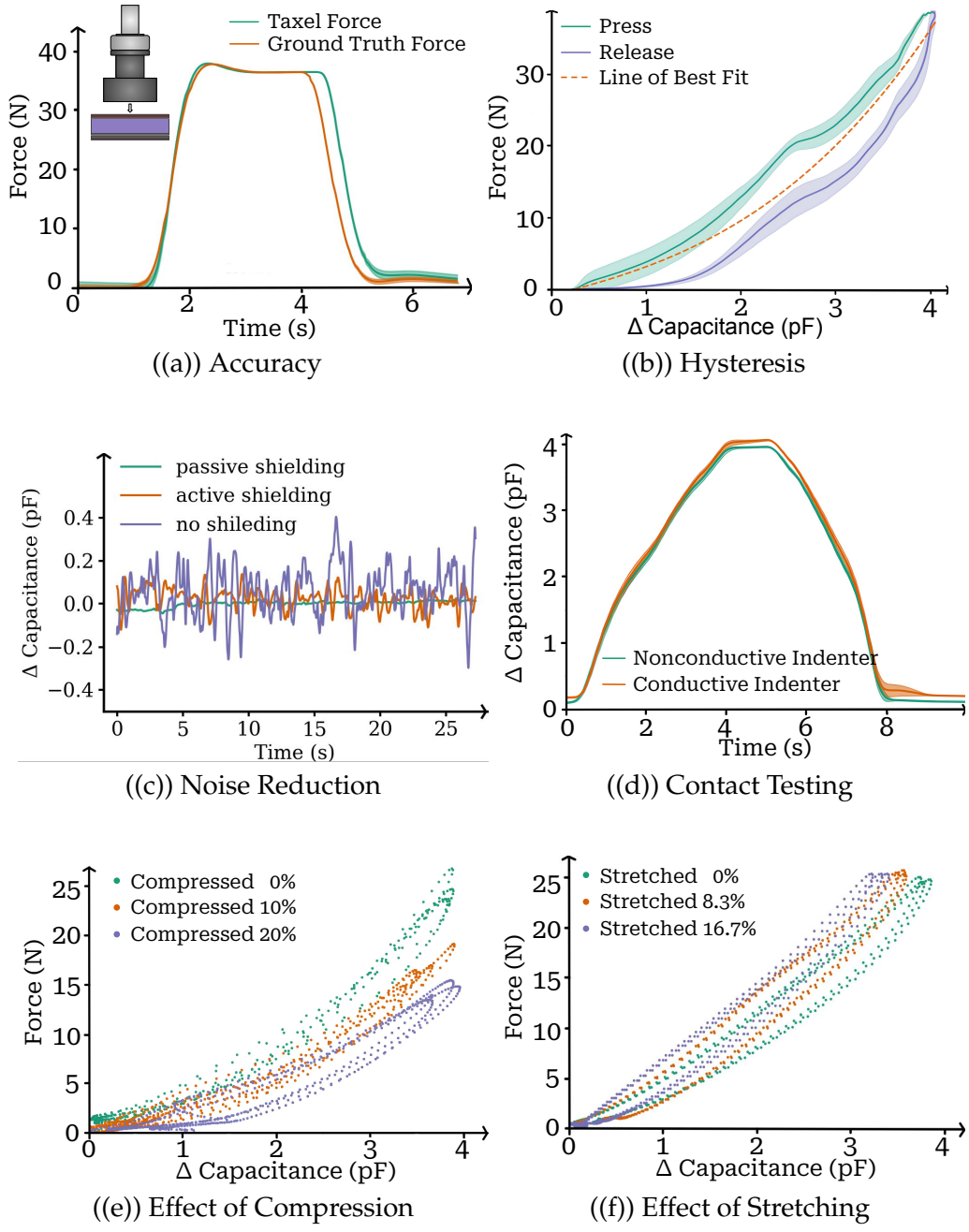

Figure 2.10: **Sensor Characteristics and Performance Evaluation.** The top-left corner of (a) shows the experiment setup comprising F/T Sensor (in light gray), Indenter (in dark gray), and the taxel (in purple). Experiment (a) validates the force-sensing capability of our skin, (b) exhibits minimal hysteresis error, (c)-(d) shows reduction of noise due to electric interference, and (e)-(f) retains sensitivity under compression and deformation.

In this section, we provide a detailed evaluation of our soft and stretchable tactile sensor. This includes an in-depth examination of its intrinsic characteristics and a comparative analysis of alternative designs.

2.4.1 Sensor Characteristics and Performance Evaluation

We conducted a detailed examination of the performance and characteristics of the proposed sensor. The following set of experiments is dedicated to unveiling the sensor's intrinsic qualities, such as precision in force measurement, repeatability, and noise reduction capability. During these experiments, we used the ATI Nano25 Force Torque (F/T) sensor to measure the ground truth force. The experiment setup is shown in Fig.2.10(a). The average measurement range of our sensor is approximately 0-5 pF, which allows it to sense forces up to 55N. The robot arm we use is the Kinova Gen3, which has a maximum payload of 8.8 lbs. While one taxel can sense up to about 12.4 lbs, a group of taxels or a section of skin can support over 100N or 22.5 lbs. Therefore, the sensing range is more than sufficient to perform the pHRI tasks and exceeds the human abdominal area pain force threshold [56].

Sensing Accuracy. To evaluate the accuracy, we compared the estimated force measurements with the ground truth values recorded by the F/T sensor. We systematically applied forces ranging from 0N to 40N and recorded both force values. Results (see Fig. 2.10(a)) show that our sensor exhibits a relative error of 0.58% with respect to the measuring range, which is low and makes it ideally suited for pHRI applications requiring accurate force feedback.

Hysteresis. Hysteresis is the phenomenon in which the sensor output de-

pends not only on the current input but also on the previous inputs. We conducted a hysteresis experiment that evaluated sensor reliability by performing 10 cycles of pressing and releasing forces. The hysteresis error (see Fig. 2.10(b)) of our sensor is 0.3 pF, about 5.4% of its measuring range. This level of error is acceptable for whole-arm sensing with ample hardware compliance like ours.

Noise Reduction and Contact Testing. Capacitive sensors are sensitive to changes in the electric field, especially near electronics and circuitry. To mitigate this interference, we employed both passive and active shielding. Our passive shielding uses highly conductive fabric to ground and isolate the sensor. Active shielding maintains potential equilibrium between the shield and the sensing layer by using the same voltage as the sensor input signal.

Fig. 2.10(c) illustrates the noise reduction of the sensor. Without shielding, the sensor detected noise is 14.2% of the measuring range. With active shielding, the noise decreased to 5.2%. The combination of active and passive shielding further reduced the noise to 3.2%, which mitigates about 77% of the noise detected by the sensor without shielding. In addition to noise reduction, shielding enables our sensor to provide consistent readings for contacts of the same magnitude, regardless of whether they are conductive or non-conductive (see Fig. 2.10(d)).

Effect of Compression. We experimented with lateral compression to assess its impact on sensor performance. We performed the tests in three groups: no compression, 10% compression, and 20% compression. In each group, we measured both the F/T sensor response and the sensor capacitance data. As shown in Fig. 2.10(e), greater compression increases the sensitivity, but our sensor retains sufficient sensitivity for force sensing in configurations where the taxels

around the joints experience lateral compression.

Effect of Stretching. We experimented with lateral stretching to assess its impact on sensor performance. We performed the tests in three groups: no stretch, stretched 8.3%, and 16.7%. In each group, we measured both the force sensor response and the sensor capacitance data. As shown in Fig. 2.10(f), lateral stretching can slightly reduce the sensitivity of the sensor but can still maintain sufficient responses to forces, which, in particular, is ideal for stable sensing around the joints of the robot.

2.4.2 Comparative Analysis of Alternative Designs

We also conduct a comparative analysis of our sensor design against alternative designs to evaluate its performance in terms of accuracy, stability, and sensitivity.

Material of Dielectric Layer. We compared soft bubble and Squishy as the dielectric layer. As shown in Fig. 2.11(a), Squishy exhibited the highest change in capacitance ΔC, indicating better sensitivity compared to the sensor with a bubble. Also, when using the bubble as the dielectric layer, occasional air leaks reduce both its cushioning and sensitivity over time. As shown in Fig. 2.11(a), we tested the sensor response when inflating the bubble with 40ml, 30ml, and 20ml of air. As the bubble deflates, the capacitance value increases, leading to a discrepancy in the calibration function.

Role of Squishy. We compared sensor readings using Squishy (**C**) as both the dielectric layer and as a soft support. Both designs offer a cushioning effect.

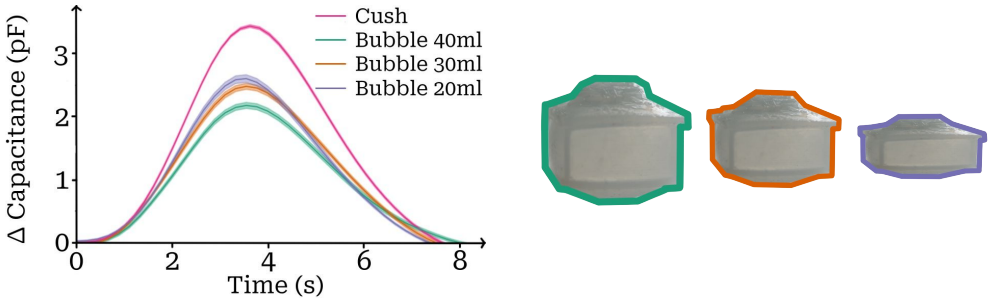

((a)) Bubble as Dielectric Material

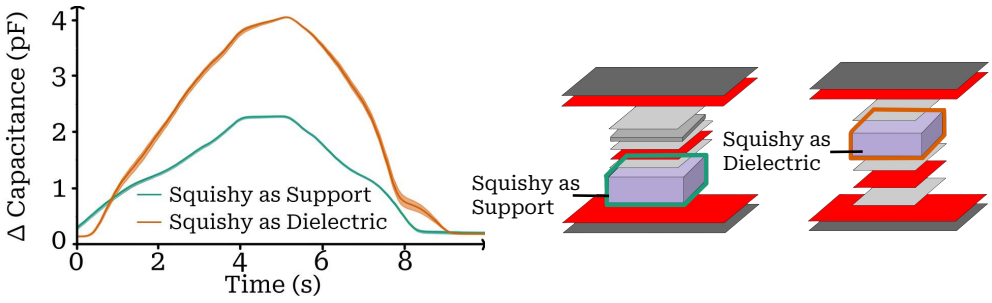

((b)) Role of Squishy Material

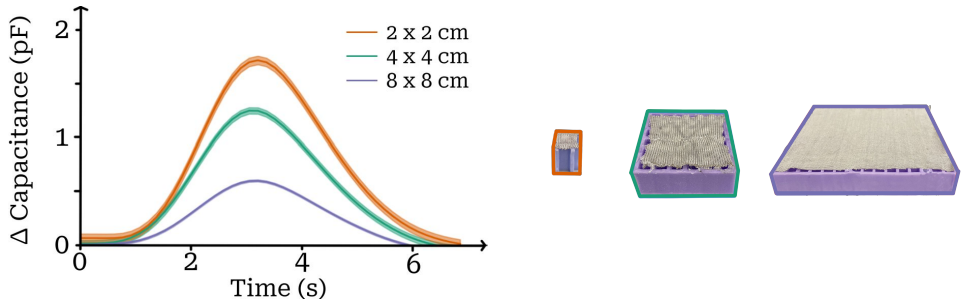

((c)) Different Size of A Taxel

Figure 2.11: **Comparative Analysis with Alternative Designs**. Experiments (a)-(b) illustrate that Squishy as a dielectric maximizes sensitivity. Smaller taxels exhibit further increases in sensitivity (c). We chose a taxel size of 4x4 cm based on a tradeoff between sensitivity and ease of construction.

In the design where Squishy serves as the dielectric layer (see Fig. 2.11(b)), ΔC is nearly double compared to when it serves as the support alone, given the same deformation. This is because, in the latter case, the dielectric layer is Scuba Fabric. This fabric is much thinner than the Squishy layer, leading to a smaller change in distance between electrodes and, therefore, a smaller ΔC.

Overall, using a thicker soft material as the dielectric layer improves the sensor sensitivity by producing a more significant change in the sensor readings.

Size of a taxel. Since our skin measures force using individual taxels, the size of a taxel matters in terms of spatial resolution. Smaller taxels provide higher resolution but may also bring more noise and a more time-consuming fabrication process. (see Fig. 2.11(c)). The sensitivity of 2cm × 2cm taxel size is almost 3 times that of 8cm × 8cm taxel size, but its noise range is about 0.04pF, which is about 4 times the 8cm × 8cm taxel. Also, the smaller the size of the taxel, the greater the complexity of fabrication. Additionally, covering the same area requires a larger number of taxels, which increases the difficulty of circuitry. So, after weighing sensitivity, resolution, noise reduction ability, and the complexity for fabrication, we finally chose 4cm × 4cm as the size of a taxel for our skin.

2.5 Capacitance Modeling And Validation

We formulated a mathematical model to predict how various actions, including Axial Compression, Lateral Compression, and Bending, impact the capacitance of our taxel-based sensor. To validate this model, we conducted a series of experiments (see Fig. 2.13). Each experiment consisted of 10 trials, and the measured capacitance is represented as an average value with a corresponding standard deviation. We assume a fixed standard deviation in the analytical values, which we model as 0.1% of the analytical capacitance. Our mathematical model is based on Eqn. 2.1, we use subscript '0' to denote the initial state and subscript '1' to denote the final state.

Axial Compression. In this scenario, force is applied to the top surface of

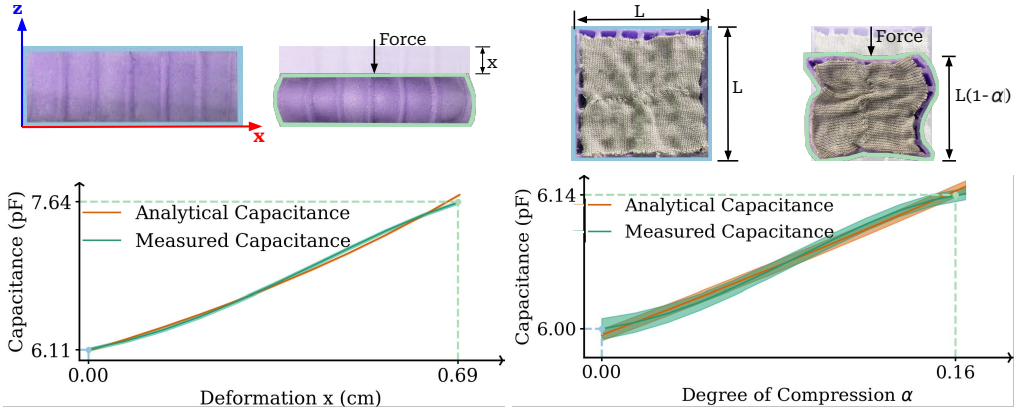

((a)) Axial Compression ((b)) Lateral Compression

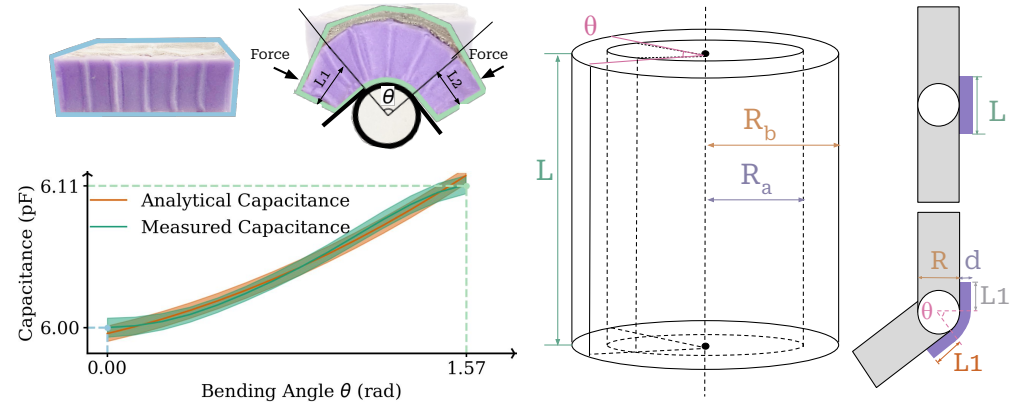

((c)) Bending ((d)) Taxel Bending Model

the taxel. Since the cross-sectional area undergoes negligible change during axial compression, we assume that the area $A = L * L$ and the permittivity ϵ remain constant. The compression causes the thickness of the dielectric layer d to decrease. Therefore, the new capacitance C_1 can be expressed as $C_0 \frac{h_0}{h_1}$. We can see from the equation that the capacitance and the thickness of the taxel after pushing are inversely proportional. The experimental result is shown in Fig. 2.12(a). The fitted mathematical model is:

$$C_1 = 5.88 \frac{1}{h_1} + 2.16 = 5.88 \frac{1}{h_0 - x} + 2.16 \tag{2.3}$$

Where x is the deformation.

Lateral Compression. Assuming horizontal forces act on the taxel and cause it to compress by a ratio of α, we express the new taxel area as $A_1 = L*L*(1-\alpha) = A_0(1-\alpha)$. Due to the grid-like structure of the dielectric layer, compressing the taxel reduces the proportion of air and increases the proportion of rubber, resulting in an overall increase in the permittivity of the dielectric layer. We postulate that this change in permittivity is linearly related to the compression ratio: $\epsilon_1 = (1 + m\alpha)\epsilon_0$, where m is a positive proportionality constant. Furthermore, when we laterally compress the taxel by 50%, the distance between the electrodes only grows by 1 mm, which is about 6% of the original distance. So, we assume that $h_1 = h_0$. Consequently, we establish:

$$\begin{aligned} C_1 &= \frac{\epsilon_0(1 + m\alpha)A_0(1 - \alpha)}{h_0} \\ &= \frac{\epsilon_0 A_0}{h_0}(1 + m\alpha - \alpha - m\alpha^2) \end{aligned} \tag{2.4}$$

We can observe that C_1 is a quadratic function of α. The experimental result is shown in Fig. 2.12(b). The fitted mathematical model is: $C_1 = 0.44\alpha^2 + 0.87\alpha + 5.99$.

Bending. When positioned between two links, the taxel bends as the joint connecting them rotates. Our model, shown in Fig. 2.12(d), divides the capacitance into bent and linear regions.

In the linear region, the taxel is firmly fixed on the joint so that the positions of its two ends on the link remain unchanged, and thus $A_L = A_{L1} + A_{L2} = A_0$. When the taxel bends, the dielectric layer stretches, leading to an increase in the proportion of air within the dielectric layer and reducing its overall permittivity. We postulate that this reduction is linearly related to the angle of bending θ, resulting in $\epsilon_1 = (1 - m\theta)\epsilon_0$. Additionally, due to the grid-like structure and the stretchable characteristic of the dielectric layer, the distance between the elec-

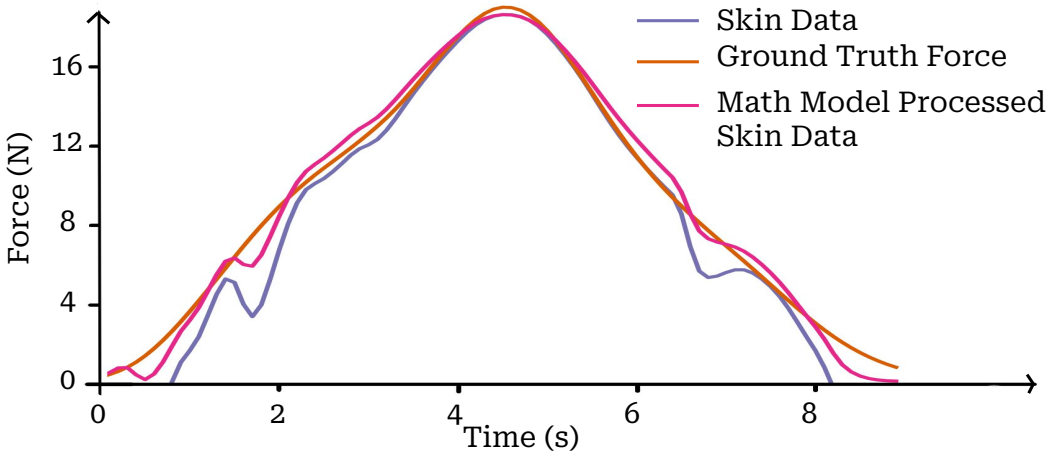

Figure 2.13: **Model-based Filtering.** Comparison of ground truth forces with skin data and the math model processed data. The processed data is obtained using *filtered* = 0.4 * *analytical* + 0.6 * *measured*, where *analytical* is calculated using the math model and *measured* is the skin data. The processed data demonstrates reduced noise and aligns well with ground truth.

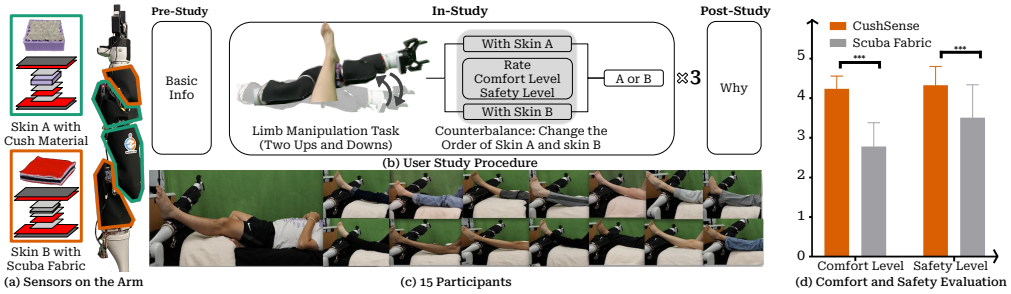

Figure 2.14: **User Study and Analysis.** Experimental setup, study procedure, and results from the limb manipulation user study evaluating the two skins' perceived safety and comfort. Most participants preferred the Cush Material over the Scuba Fabric. *** indicates significant differences with $p_{0.0001}$.

trodes remains almost unchanged when we bend the taxel. Therefore, we assume $h_1 = h_0$. Consequently, the capacitance of the cumulative linear region can be expressed as $C_L = \frac{\epsilon_0(1 - m\theta)A_0}{h_0} = C_0(1 - m\theta)$. When considering the bent region, we use a cylindrical capacitor model, as shown in Fig. 2.12(d). This model represents a cylindrical capacitor of length L formed by an inner and an outer conductive cylindrical shell with radii R_a and R_b, respectively. The capacitance of the cylindrical capacitor can be expressed as $C = \frac{2\pi\epsilon L}{ln(R_b/R_a)}$. In case of the capacitance of the bent region, $R_b = R_a + d$, $\epsilon = (1 - \theta)\epsilon_0$, and the capacitance

only takes $\theta/2\pi$ of the capacitor value of the entire cylindrical model. So, the capacitance of the bending region is:

$$C_B = \frac{2\pi\epsilon_0(1-m\theta)L}{ln(1+d/R_a)}\frac{\theta}{2\pi} = \frac{\epsilon_0 L}{ln(1+d/R_a)}(\theta - m\theta^2) \tag{2.5}$$

Thus, the total capacitance of the taxel would be the sum of C_B and C_L:

$$\begin{aligned} C_{total} &= C_B + C_L \\ &= C_0(1-m\theta) + \frac{\epsilon_0 L}{ln(1+d/R_a)}(\theta - m\theta^2) \\ &= a\theta^2 + b\theta + c \end{aligned} \tag{2.6}$$

where a, b, c are proportionality constants given by the physical parameters of the taxel. The experimental result is shown in Fig. 2.12(c). The fitted mathematical model is: $C_1 = 0.024\theta^2 + 0.041\theta + 5.99$.

This model serves a dual purpose: 1) validating the proper fabrication of taxels, and 2) using the analytical values for better filtering of measured capacitance in high-noise environments (see Fig. 2.13). Building upon this, there is potential in the future to devise control policies that leverage this model as a predictive tool, dynamically accounting for parameters like deformation and bending angle, thereby enhancing robots' capabilities in complex contact-rich interactions.

2.6 User Study

Providing physical assistance for ADLs, such as dressing, bathing, and transferring, often involves limb manipulation [57, 58] as a critical task. To evaluate the perceived safety and comfort of our tactile skin during pHRI, we centered our

user study around limb manipulation. We recruited 15 human subjects (9 Female, 6 Male) to participate in our study. Their mean age was 22.27 years (SD = 4.11), and their mean weight was 137.73 lb (SD = 32.98). Of all the participants, 40% had previous experience with robots.

2.6.1 Experimental Setup

The main source of comfort in CushSense is the dielectric material. To demonstrate how it affects perceived safety and comfort, we compared our sensor with an alternate version, where we replaced the dielectric layer with Scuba Fabric (see Fig. 2.14). We chose the Scuba Fabric since it is stretchable and soft yet does not offer the same degree of cushioning. During the study, the robot arm was positioned under the ankle of the participants.

2.6.2 Experimental Procedure

Participants lay on a bed with their eyes blindfolded and shoes removed. Their ankles were placed against one of the two skins. The robot arm raised their left leg, maintained the position for 5 seconds, and gently lowered it. This process was repeated twice for each skin. The participants then evaluated the comfort and safety of each skin and rated them based on the following criteria:

- **Comfort level**: Participants rated their comfort on a five-point scale: *very comfortable*, *comfortable*, *neutral*, *uncomfortable*, and *very uncomfortable*.
- **Safety level**: We assessed the safety using a similar five-point scale: *very safe*, *safe*, *neutral*, *unsafe*, and *very unsafe*.

The entire procedure was repeated three times, with the order of skin types counterbalanced to improve the methodological credibility. Detailed information on the user study questionnaire can be found on our website [55]. The study protocol was reviewed and approved by the Institutional Review Board at Cornell University (Protocol #IRB0146211). All participants provided written informed consent to participate in the study.

2.6.3 Results and Discussion

14 out of 15 participants preferred CushSense over the Scuba Fabric version. A summarized comparison is available in Fig. 2.14. Overall, the evaluations highlight a consistent inclination towards the comfort and safety offered by CushSense compared to the Scuba Fabric. This consensus among participants is evident from the lower variance in the evaluations for our tactile skin. A subsequent paired sample t-test on the comfort and safety ratings verified significant distinctions between CushSense and Scuba Fabric. In summary, our soft and well-cushioned skin elevates the user experience in terms of comfort and safety. This improvement holds significant promise for pHRI in fields such as the assistance of people with mobility limitations and elderly care.

CHAPTER 3

CONCLUSIONS AND FUTURE DIRECTIONS

3.0.1 Conclusion

The main contributions of this paper include:

- We design and fabricate a whole-arm soft and stretchable tactile-sensing skin.
- We perform sensor characterization to demonstrate the sensing advantages of the proposed sensor design.
- We demonstrate the superior perceived safety and comfort of our sensor through a pHRI user study.
- We release open-source hardware, including the design files, fabrication process, calibration, and visualization utilities for the skin.

CushSense provides a convenient way of making rigid robots safer without sacrificing manipulability. With our open-source hardware, we hope to see more robots that are soft and comfortable to interact with.

3.0.2 Future Work

Flexible PCBs could represent a future direction for skin development. During our user study, we observed that the rigid PCB often became a point of discomfort for users. By transitioning to flexible PCBs, the board thickness could be reduced from 1.6 mm to 0.1 mm, potentially enhancing user comfort.

Another avenue for future exploration is the development of an algorithm for automatic calibration and taring of the skin. In our current design, manual taring is required. However, during user interactions, certain sensors activate without direct contact, a phenomenon often referred to as sensor ghosting. This can be attributed to movements in the user's ankle and the hardware components of the skin. Exploring more secure methods of affixing wires and boards to the robot arm is also worth considering.

One limitation of our work is the non-trivial weight of CushSense, which could place additional demands on the controller and hardware when applied to the entire body. Additionally, CushSense is tailored for a specific robot arm, rather than offering a universal fit.

To address these challenges, future work could focus on reducing the polymer density to decrease weight. Additionally, adopting a cut and conformal structure might enable the transformation of any robot into a soft robot.

APPENDIX A

APPENDIX A

Bill of Materials

PCBs	Qty	Unit Price	Total Price	URL	Description	Cost / taxel	Qty / taxel	Qty in 56 taxels	cost
Texas Instrument	74	$7.48	$553.52	https://www.mous	FDC1004DGSR			16	$119.68
TDK 0.1uF 0603	80	$0.10	$8.00	https://www.mous	C0603X5R1E104K030BB			1	$0.10
YAGEO 1uF 060	80	$0.11	$8.80	https://www.mous	CC0603KRX5R8BB105			3	$0.33
Kyocera AVX 51p	150	$0.45	$67.50	https://www.mous	06033A510FAT2A			0	$0.00
Vishay 4.99kOhn	150	$0.12	$18.15	https://www.mous	RCC06034K99FKEA			2	$0.24
Texas Instrument	10	$6.95	$69.50	https://www.adafr	TCA9548A			4	$27.80
Molex 4-pos Mole	9	$5.26	$47.34	https://www.digik	1451300401			4	$21.04
Molex Onboard p	20	$1.42	$28.40	https://www.digik	1053131104			8	$11.36
CDC	3	0.6	1.8		plain PCB ordered from OSH park			16	9.6
Multiplexer	3	1.466666667	4.4		plain PCB ordered from OSH park			4	5.866666667
Controller									
arduino nano 3 p	1	$25.99	$25.99	https://www.amazon.com/ELEGOO-Arduino-ATmega328P-Without-Compatible/dp/B071				1	$25.99
multiplexer	9	$6.95	$62.55	https://learn.adafruit.com/adafruit-tca9548a-1-to-8-i2c-multiplexer-breakout/circuitpythor				4	$27.80
Fabric									
Strech conductiv	10	$44.99	$449.90	https://lessemf.cc	highly conductive fabric	0.3576			20.0256
SILVERELL® FA	5	$40.00	$200.00	https://lessemf.cc	silverell fabric	0.4			22.4
Nylon spandex fa	3	$10.99	$32.97	https://www.amaz	non conductive fabric	0.0499			2.7944
Misc									
ring connector	100	$0.14	$14.04	https://www.digikey.com/en/products/detail/te-connectivity-amp-conne			3	168	$23.52
1.25mm Pitch 4-p	100	$0.76	$76.00	https://www.adafr	connectors from mux to CDC			16	$12.16
purple squishy	1	$30.00	$30.00	https://purple.cor	dielectric material 30pk	1		56	56
E6000 clear glue	1	3.49	3.49	https://www.joann.com/e-6000/4357455.html?gclid=CjwKCAjwgZCoBhBnEiwAz35Rwta				**Total**	$386.71
								avg cost/taxel	$6.91

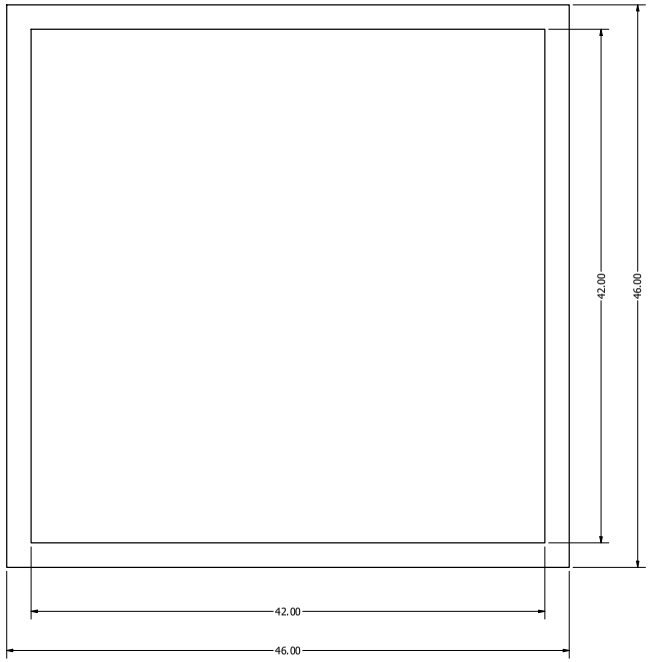

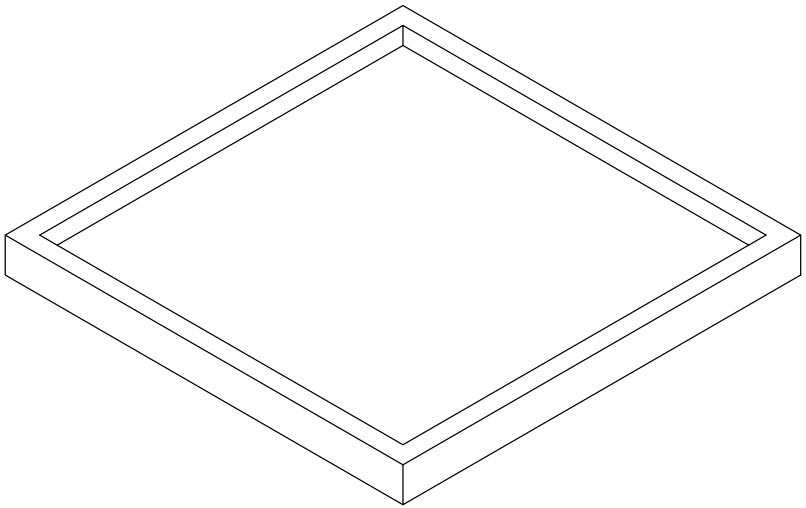

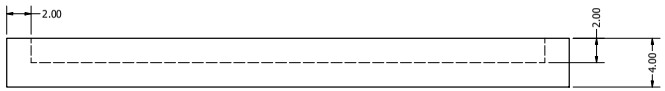

DRAWN YYQ	10/9/2023		
CHECKED		TITLE	
QA			
MFG			
APPROVED		SIZE D	DWG NO airbubble_mold_bottom REV
		SCALE 5 : 1	SHEET 1 OF 1

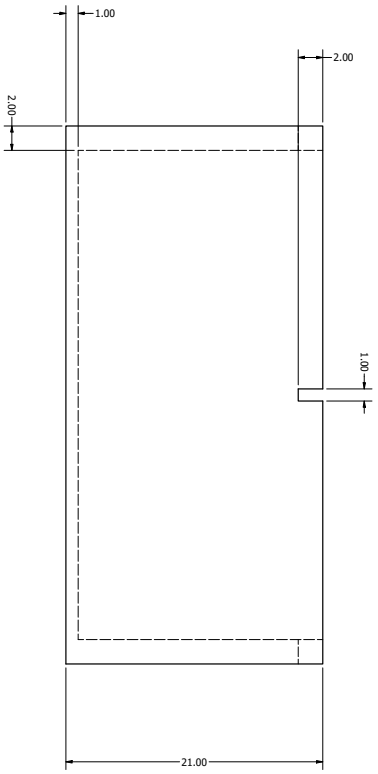

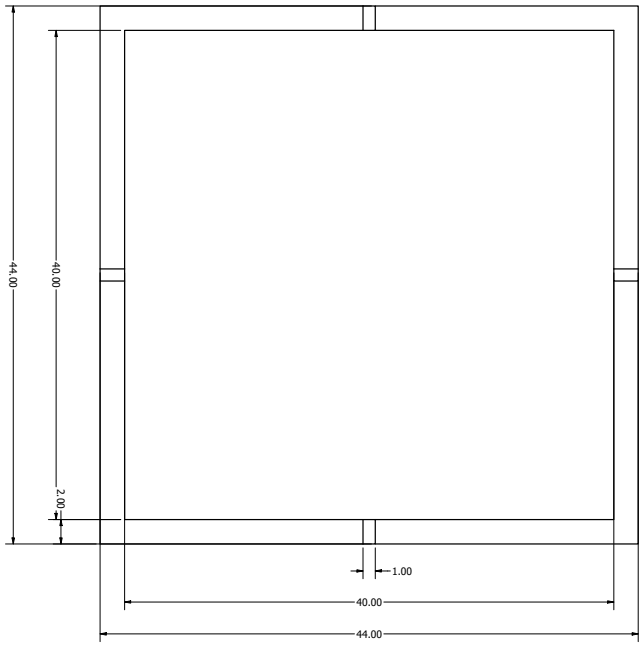

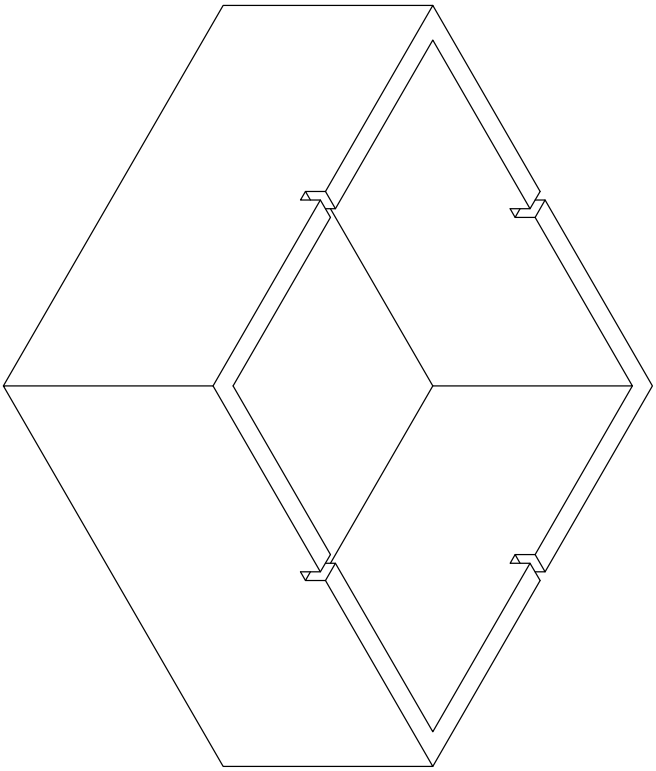

						DRAWN	
						CHECKED	YTQ
						QA	
						MFG	
						APPROVED	
							10/6/2023
SCALE	SIZE					TITLE	
5 : 1	D						
SHEET 1 OF 1	DWG NO	airbubble_mold_outter					
	REV						

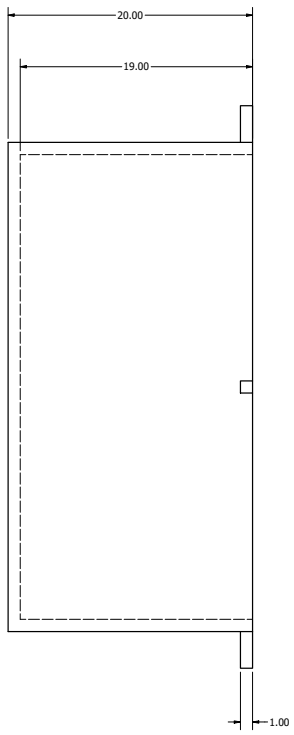

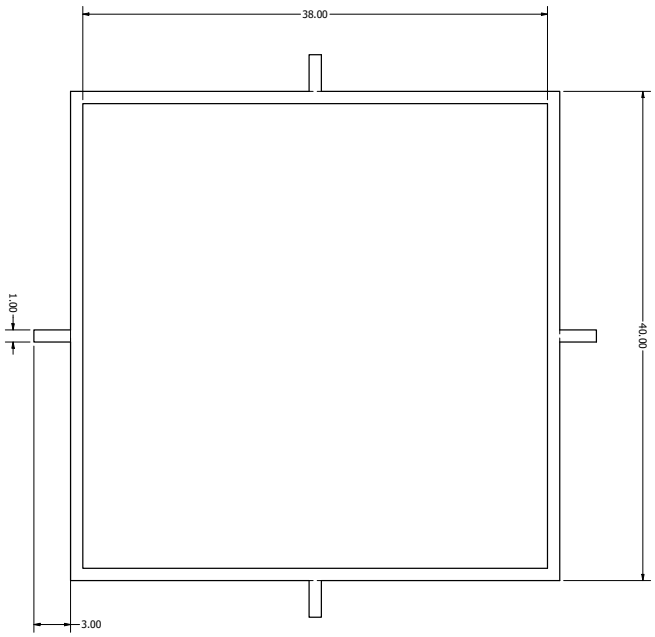

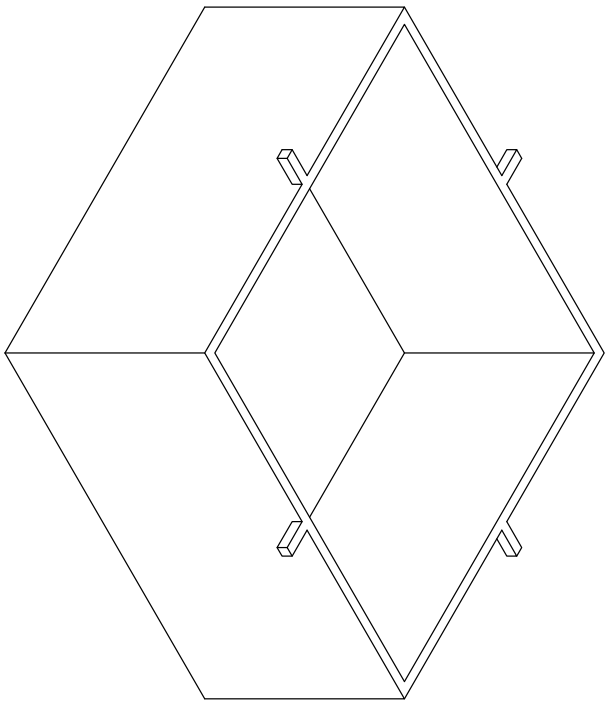

DRAWN	YTQ		
CHECKED		10/9/2023	
QA			
MFG			
APPROVED			
SIZE	D	TITLE	
SCALE	5 : 1		
DWG NO	softMold_in		
REV			
SHEET 1 OF 1			

BIBLIOGRAPHY

[1] "Arduino capacitivesensor library website." https://playground.arduino.cc/Main/CapacitiveSensor.

[2] S. Abdi, I. Kitsara, M. S. Hawley, and L. de Witte, "Emerging technologies and their potential for generating new assistive technologies," *Assistive Technology*, vol. 33, no. sup1, pp. 17–26, 2021.

[3] P. M. Grice, M. D. Killpack, A. Jain, S. Vaish, J. Hawke, and C. C. Kemp, "Whole-arm tactile sensing for beneficial and acceptable contact during robotic assistance," in *2013 IEEE 13th International Conference on Rehabilitation Robotics (ICORR)*, pp. 1–8, IEEE, 2013.

[4] A. Jain, M. D. Killpack, A. Edsinger, and C. C. Kemp, "Reaching in clutter with whole-arm tactile sensing," *The International Journal of Robotics Research*, vol. 32, no. 4, pp. 458–482, 2013.

[5] P. Mittendorfer, E. Yoshida, and G. Cheng, "Realizing whole-body tactile interactions with a self-organizing, multi-modal artificial skin on a humanoid robot," *Advanced Robotics*, vol. 29, no. 1, pp. 51–67, 2015.

[6] T. Bhattacharjee, A. Jain, S. Vaish, M. D. Killpack, and C. C. Kemp, "Tactile sensing over articulated joints with stretchable sensors," in *2013 World Haptics Conference (WHC)*, pp. 103–108, IEEE, 2013.

[7] G. Cheng, E. Dean-Leon, F. Bergner, J. R. G. Olvera, Q. Leboutet, and P. Mittendorfer, "A comprehensive realization of robot skin: Sensors, sensing, control, and applications," *Proceedings of the IEEE*, vol. 107, no. 10, pp. 2034–2051, 2019.

[8] Y. Zhou, J. Zhao, P. Lu, Z. Wang, and B. He, "Tacsuit: A wearable large-area, bioinspired multi-modal tactile skin for collaborative robots," *IEEE Transactions on Industrial Electronics*, 2023.

[9] Z. Si, T. C. Yu, K. Morozov, J. McCann, and W. Yuan, "Robotsweater: Scalable, generalizable, and customizable machine-knitted tactile skins for robots," *arXiv preprint arXiv:2303.02858*, 2023.

[10] W. Bottcher, P. Machado, N. Lama, and T. M. McGinnity, "Object recognition for robotics from tactile time series data utilising different neural network architectures," in *2021 International Joint Conference on Neural Networks (IJCNN)*, pp. 1–8, IEEE, 2021.

[11] D. Guo, F. Sun, B. Fang, C. Yang, and N. Xi, "Robotic grasping using visual and tactile sensing," *Information Sciences*, vol. 417, pp. 274–286, 2017.

[12] X. A. Wu, T. M. Huh, A. Sabin, S. A. Suresh, and M. R. Cutkosky, "Tactile sensing and terrain-based gait control for small legged robots," *IEEE Transactions on Robotics*, vol. 36, no. 1, pp. 15–27, 2019.

[13] A. Goncalves, N. Kuppuswamy, A. Beaulieu, A. Uttamchandani, K. M. Tsui, and A. Alspach, "Punyo-1: Soft tactile-sensing upper-body robot for large object manipulation and physical human interaction," in *2022 IEEE 5th International Conference on Soft Robotics (RoboSoft)*, pp. 844–851, IEEE, 2022.

[14] L. Jamone, L. Natale, G. Metta, and G. Sandini, "Highly sensitive soft tactile sensors for an anthropomorphic robotic hand," *IEEE sensors Journal*, vol. 15, no. 8, pp. 4226–4233, 2015.

[15] T. Paulino, P. Ribeiro, M. Neto, S. Cardoso, A. Schmitz, J. Santos-Victor, A. Bernardino, and L. Jamone, "Low-cost 3-axis soft tactile sensors for the human-friendly robot vizzy," in *2017 IEEE international conference on robotics and automation (ICRA)*, pp. 966–971, IEEE, 2017.

[16] E. Donlon, S. Dong, M. Liu, J. Li, E. Adelson, and A. Rodriguez, "Gelslim: A high-resolution, compact, robust, and calibrated tactile-sensing finger," in *2018 IEEE/RSJ International Conference on Intelligent Robots and Systems (IROS)*, pp. 1927–1934, IEEE, 2018.

[17] Y. Yan, Z. Hu, Z. Yang, W. Yuan, C. Song, J. Pan, and Y. Shen, "Soft magnetic skin for super-resolution tactile sensing with force self-decoupling," *Science Robotics*, vol. 6, no. 51, p. eabc8801, 2021.

[18] T. Hellebrekers, O. Kroemer, and C. Majidi, "Soft magnetic skin for continuous deformation sensing," *Advanced Intelligent Systems*, vol. 1, no. 4, p. 1900025, 2019.

[19] R. Bhirangi, T. Hellebrekers, C. Majidi, and A. Gupta, "Reskin: versatile, replaceable, lasting tactile skins," *arXiv preprint arXiv:2111.00071*, 2021.

[20] W. Yuan, S. Dong, and E. H. Adelson, "Gelsight: High-resolution robot tactile sensors for estimating geometry and force," *Sensors*, vol. 17, no. 12, p. 2762, 2017.

[21] M. Lambeta, P.-W. Chou, S. Tian, B. Yang, B. Maloon, V. R. Most, D. Stroud, R. Santos, A. Byagowi, G. Kammerer, *et al.*, "Digit: A novel design for a low-cost compact high-resolution tactile sensor with application to in-hand manipulation," *IEEE Robotics and Automation Letters*, vol. 5, no. 3, pp. 3838–3845, 2020.

[22] N. Kuppuswamy, A. Alspach, A. Uttamchandani, S. Creasey, T. Ikeda, and R. Tedrake, "Soft-bubble grippers for robust and perceptive manipulation," in *2020 IEEE/RSJ International Conference on Intelligent Robots and Systems (IROS)*, pp. 9917–9924, IEEE, 2020.

[23] G. Zhang, Y. Du, Y. Zhang, and M. Y. Wang, "A tactile sensing foot for single robot leg stabilization," in *2021 IEEE International Conference on Robotics and Automation (ICRA)*, pp. 14076–14082, IEEE, 2021.

[24] I. Huang and R. Bajcsy, "High resolution soft tactile interface for physical human-robot interaction," in *2020 IEEE International Conference on Robotics and Automation (ICRA)*, pp. 1705–1711, 2020.

[25] D. P. Cotton, I. M. Graz, and S. P. Lacour, "A multifunctional capacitive sensor for stretchable electronic skins," *IEEE Sensors Journal*, vol. 9, no. 12, pp. 2008–2009, 2009.

[26] Z. Ji, H. Zhu, H. Liu, T. Chen, and L. Sun, "A flexible capacitive tactile sensor for robot skin," in *2016 International Conference on Advanced Robotics and Mechatronics (ICARM)*, pp. 207–212, 2016.

[27] T.-H.-L. Le, A. Maslyczyk, J.-P. Roberge, and V. Duchaine, "A highly sensitive multimodal capacitive tactile sensor," in *2017 IEEE International Conference on Robotics and Automation (ICRA)*, pp. 407–412, 2017.

[28] W. Xiong, H. Feng, H. Liwang, D. Li, W. Yao, D. Duolikun, Y. Zhou, and Y. Huang, "Multifunctional tactile feedbacks towards compliant robot manipulations via 3d-shaped electronic skin," *IEEE Sensors Journal*, vol. 22, no. 9, pp. 9046–9056, 2022.

[29] J. A. Fishel and G. E. Loeb, "Sensing tactile microvibrations with the biotac — comparison with human sensitivity," in *2012 4th IEEE RAS & EMBS International Conference on Biomedical Robotics and Biomechatronics (BioRob)*, pp. 1122–1127, 2012.

[30] D. M. Vogt, Y.-L. Park, and R. J. Wood, "Design and characterization of a soft multi-axis force sensor using embedded microfluidic channels," *IEEE Sensors Journal*, vol. 13, no. 10, pp. 4056–4064, 2013.

[31] T. Kim and Y.-L. Park, "A soft three-axis load cell using liquid-filled three-dimensional microchannels in a highly deformable elastomer," *IEEE robotics and automation letters*, vol. 3, no. 2, pp. 881–887, 2018.

[32] X. Shi, C.-H. Cheng, Y. Zheng, and P. K. A. Wai, "An egain-based flexible piezoresistive shear and normal force sensor with hysteresis analysis in normal force direction," *Journal of Micromechanics and Microengineering*, vol. 26, no. 10, p. 105020, 2016.

[33] M. Inaba, Y. Hoshino, K. Nagasaka, T. Ninomiya, S. Kagami, and H. Inoue, "A full-body tactile sensor suit using electrically conductive fabric and strings," in *Proceedings of IEEE/RSJ International Conference on Intelligent Robots and Systems. IROS'96*, vol. 2, pp. 450–457, IEEE, 1996.

[34] R. Kageyama, S. Kagami, M. Inaba, and H. Inoue, "Development of soft and distributed tactile sensors and the application to a humanoid robot," in *IEEE SMC'99 Conference Proceedings. 1999 IEEE International Conference on Systems, Man, and Cybernetics (Cat. No.99CH37028)*, vol. 2, pp. 981–986 vol.2, 1999.

[35] T. Mukai, M. Onishi, T. Odashima, S. Hirano, and Z. Luo, "Development

of the tactile sensor system of a human-interactive robot "ri-man"," *IEEE Transactions on robotics*, vol. 24, no. 2, pp. 505–512, 2008.

[36] T. Yoshikai, H. Fukushima, M. Hayashi, and M. Inaba, "Development of soft stretchable knit sensor for humanoids' whole-body tactile sensibility," in *2009 9th IEEE-RAS International Conference on Humanoid Robots*, pp. 624–631, IEEE, 2009.

[37] J. Wade, T. Bhattacharjee, R. D. Williams, and C. C. Kemp, "A force and thermal sensing skin for robots in human environments," *Robotics and Autonomous Systems*, vol. 96, pp. 1–14, 2017.

[38] Y. Luo, Y. Li, P. Sharma, W. Shou, K. Wu, M. Foshey, B. Li, T. Palacios, A. Torralba, and W. Matusik, "Learning human–environment interactions using conformal tactile textiles," *Nature Electronics*, vol. 4, no. 3, pp. 193–201, 2021.

[39] Z. Ye, G. Pang, K. Xu, Z. Hou, H. Lv, Y. Shen, and G. Yang, "Soft robot skin with conformal adaptability for on-body tactile perception of collaborative robots," *IEEE Robotics and Automation Letters*, vol. 7, no. 2, pp. 5127–5134, 2022.

[40] P. Mittendorfer and G. Cheng, "Humanoid multimodal tactile-sensing modules," *IEEE Transactions on robotics*, vol. 27, no. 3, pp. 401–410, 2011.

[41] J. Ulmen and M. Cutkosky, "A robust, low-cost and low-noise artificial skin for human-friendly robots," in *2010 IEEE International conference on robotics and automation*, pp. 4836–4841, IEEE, 2010.

[42] P. Maiolino, M. Maggiali, G. Cannata, G. Metta, and L. Natale, "A flexible

and robust large scale capacitive tactile system for robots," *IEEE Sensors Journal*, vol. 13, no. 10, pp. 3910–3917, 2013.

[43] D. Hughes, J. Lammie, and N. Correll, "A robotic skin for collision avoidance and affective touch recognition," *IEEE Robotics and Automation Letters*, vol. 3, no. 3, pp. 1386–1393, 2018.

[44] M. Teyssier, B. Parilusyan, A. Roudaut, and J. Steimle, "Human-like artificial skin sensor for physical human-robot interaction," in *2021 IEEE International Conference on Robotics and Automation (ICRA)*, pp. 3626–3633, 2021.

[45] A. Alspach, J. Kim, and K. Yamane, "Design of a soft upper body robot for physical human-robot interaction," in *2015 IEEE-RAS 15th International Conference on Humanoid Robots (Humanoids)*, pp. 290–296, IEEE, 2015.

[46] T. Kim, J. Park, S. J. Yoon, H.-W. Park, Y.-L. Park, *et al.*, "Design of a lightweight inflatable sensing sleeve for increased adaptability and safety of legged robots," in *2019 2nd IEEE International Conference on Soft Robotics (RoboSoft)*, pp. 257–264, IEEE, 2019.

[47] D. Kim, S. Han, T. Kim, C. Kim, D. Lee, D. Kang, and J.-S. Koh, "Design of a sensitive balloon sensor for safe human–robot interaction," *Sensors*, vol. 21, no. 6, p. 2163, 2021.

[48] L. Van Duong and V. A. Ho, "Large-scale vision-based tactile sensing for robot links: Design, modeling, and evaluation," *IEEE Transactions on Robotics*, vol. 37, no. 2, pp. 390–403, 2021.

[49] Q. K. Luu, N. H. Nguyen, *et al.*, "Simulation, learning, and application of vision-based tactile sensing at large scale," *IEEE Transactions on Robotics*, 2023.

[50] O. Atalay, "Textile-based, interdigital, capacitive, soft-strain sensor for wearable applications," *Materials*, vol. 11, no. 5, 2018.

[51] M. B. H. Othman, M. R. Ramli, L. Y. Tyng, Z. Ahmad, and H. M. Akil, "Dielectric constant and refractive index of poly (siloxane–imide) block copolymer," *Materials & Design*, vol. 32, no. 6, pp. 3173–3182, 2011.

[52] R. Salvado, C. Loss, R. Gonçalves, and P. Pinho, "Textile materials for the design of wearable antennas: A survey," *Sensors*, vol. 12, no. 11, pp. 15841–15857, 2012.

[53] Z. Ahmad, "Polymer dielectric materials," in *Dielectric Material* (M. A. Silaghi, ed.), ch. 1, Rijeka: IntechOpen, 2012.

[54] R. F. Shepherd, F. Ilievski, W. Choi, S. A. Morin, A. A. Stokes, A. D. Mazzeo, X. Chen, M. Wang, and G. M. Whitesides, "Multigait soft robot," *Proceedings of the national academy of sciences*, vol. 108, no. 51, pp. 20400–20403, 2011.

[55] "CushSense website." https://sites.google.com/cornell.edu/cushsense.

[56] R. Behrens, G. Pliske, M. Umbreit, S. Piatek, F. Walcher, and N. Elkmann, "A statistical model to determine biomechanical limits for physically safe interactions with collaborative robots," *Frontiers in robotics and AI*, vol. 8, p. 667818, 2022.

[57] K. Chow and C. C. Kemp, "Robotic repositioning of human limbs via model predictive control," in *2016 25th IEEE International Symposium on Robot and Human Interactive Communication (RO-MAN)*, pp. 473–480, 2016.

[58] R. Madan, R. K. Jenamani, V. T. Nguyen, A. Moustafa, X. Hu, K. Dimitropoulou, and T. Bhattacharjee, "Sparcs: Structuring physically assistive

robotics for caregiving with stakeholders-in-the-loop," in *2022 IEEE/RSJ International Conference on Intelligent Robots and Systems (IROS)*, pp. 641–648, IEEE, 2022.